Ultrahigh Tunability of Room Temperature Electronic Transport and Ferromagnetism in Dilute Magnetic Semiconductor and PMN-PT Single-Crystal-Based Field Effect Transistors via Electric Charge Mediation

Qiu-Xiang Zhu, Ming-Min Yang, Ming Zheng, Ren-Kui Zheng, Li-Jie Guo, Yu Wang, Jin-Xing Zhang, Xiao-Min Li,* Hao-Su Luo, and Xiao-Guang Li*

Multiferroic heterostructures composed of complex oxide thin films and ferroelectric single crystals have aroused considerable interest due to the electrically switchable strain and charge elements of oxide films by the polarization reversal of ferroelectrics. Previous studies have demonstrated that the electric-field-control of physical properties of such heterostructures is exclusively due to the ferroelectric domain switching-induced lattice strain effects. Here, the first successful integration of the hexagonal ZnO:Mn dilute magnetic semiconductor thin films with high performance (111)-oriented perovskite $Pb(Mg_{1/3}Nb_{2/3})O_3$-$PbTiO_3$ (PMN-PT) single crystals is reported, and unprecedented charge-mediated electric-field control of both electronic transport and ferromagnetism at room temperature for PMN-PT single crystal-based oxide heterostructures is realized. A significant carrier concentration-tunability of resistance and magnetization by ≈400% and ≈257% is achieved at room temperature. The electric-field controlled bistable resistance and ferromagnetism switching at room temperature via interfacial electric charge presents a potential strategy for designing prototype devices for information storage. The results also disclose that the relative importance of the strain effect and interfacial charge effect in oxide film/ferroelectric crystal heterostructures can be tuned by appropriately adjusting the charge carrier density of oxide films.

1. Introduction

Reversible and nonvolatile manipulation of magnetization and resistance (the most important properties in spintronic apparatus) has sparked a surge of research activities in the last decade due to its fundamental importance and potential applications in memory industry. Particularly, an electric control of functionalities that allows faster and lower-power operations has attracted growing concern.[1–7] Advancements in mature thin-film fabrication technologies have enabled the synthesis of high quality complex oxide/ferroelectric (FE) heterostructures where the ferroelectric polarization can be utilized to reversibly modulate the properties of oxide films. There are two major mechanisms in this class of heterostructures: strain effect and ferroelectric field effect. Upon ferroelectric poling or polarization switching, the induced strain in the FE layer can be in situ transferred to the oxide film, thus tuning the lattice strain, magnetization, and resistance of the films.[7–11] However, retaining the induced strain after removing the electric field still remains a challenge. Recently, two reversible and stable remnant strain states have been achieved by applying an electric field with appropriate magnitude (less than the coercive field of FE layer) to the FE layer with a particular crystal orientation, e.g., (011)-oriented (1-x)$Pb(Mg_{1/3}Nb_{2/3})O_3$-$x PbTiO_3$ crystal.[8,11] Unfortunately, the corresponding variations in magnetization (<3% at 300 K) and resistance (<3% at 300 K) are

Dr. Q.-X. Zhu, Dr. M.-M. Yang, Dr. M. Zheng, Prof. R.-K. Zheng,
Prof. X.-M. Li, Prof. H.-S. Luo
State Key Laboratory of High Performance Ceramics
and Superfine Microstructure
Shanghai Institute of Ceramics
Chinese Academy of Sciences
Shanghai 200050 China
E-mail: zrk@ustc.edu; lixm@mail.sic.ac.cn

Dr. L.-J. Guo, Prof. J.-X. Zhang
Department of Physics
Beijing Normal University
Beijing 100875, China

Prof. Y. Wang
Department of Applied Physics
The Hong Kong Polytechnic University
Hong Kong, China

Prof. X.-G. Li
Hefei National Laboratory for Physical Sciences
at Microscale and Department of Physics
University of Science and Technology of China
Hefei 230026, China

DOI: 10.1002/adfm.201403763

rather small,[8,11] thus unfavorable for practical applications. On the other hand, the ferroelectric field effect, where the oxide film and the FE layer respectively act as the conductive channel and the insulating gate (i.e., ferroelectric field effect transistors, FETs), respectively, offers the possibility of reversible and nonvolatile switching of magnetization and resistance due to dual remnant polarization in the absence of externally applied electric field.[12] The electric polarization of ferroelectrics attracts or repels charge carriers, creating a thin charge accumulation or depletion layer at the interface that modifies the charge-related electronic transport and magnetic properties of channel.[13]

Strongly correlated complex oxides, including high-temperature superconducting cuprates,[14] colossal magnetoresistive manganites,[8,9,15–17] and nickelates,[18] have been integrated with perovskite-type ferroelectrics (e.g., $BiFeO_3$, $BaTiO_3$, $PbZr_{0.52}Ti_{0.48}O_3$) to tailor or realize exotic magnetic and electronic phases. In doped manganites on account of lattice strain as well as carrier concentration dependence of electronic transport and magnetic properties, for example, the ferroelectric field effect can only be observed when it is not dominated over by the strain effect and can be achieved by choosing an appropriate doping level of manganites, that is, in the vicinity of phase boundary (e.g., half-doped $La_{0.5}Ca_{0.5}MnO_3$[17,18]) and/or by decreasing film thickness and/or by reducing the temperature.[16] However, these factors impose severe constraints for practical device applications of FETs. Therefore, it would be essential to seek other candidates that are more susceptible to ferroelectric field effect than strain effect at room temperature. Mn-doped ZnO (ZnO:Mn), one of the outstanding dilute magnetic semiconductors (DMSs) with potential applications for future spintronic apparatus, is an alternative channel material because of its distinctive electronic and magnetic properties. In particular, the properties of ZnO:Mn have proven to be carrier concentration-tunable.[19] This presents an opportunity to design field effect devices with magnetization and resistance that may be tuned both electrically and magnetically in a reversible, nonvolatile, and reproducible manner at room temperature.

In addition to the above stringent requirements on channel materials, one of the other crucial factors for effective device performance is the large remnant polarization of the ferroelectrics.[13,20] Perovskite $(1\text{-}x)Pb(Mg_{1/3}Nb_{2/3})O_3\text{-}xPbTiO_3$ (PMN-xPT) single crystals exhibit excellent ferroelectric and piezoelectric activities and have been widely used to grow complex oxide films, e.g., $La_{0.7}Sr_{0.3}CoO_3$/PMN-xPT,[21] $La_{1-x}A_xMnO_3$/PMN-xPT (A = Ca, Sr, Ba),[8,9,11,15,22,23] VO_2/PMN-xPT,[24,25] Fe_3O_4/PMN-xPT,[7] $CoFe_2O_4$/PMN-xPT,[26,27] and $BiFeO_3$/$La_{0.7}Sr_{0.3}MnO_3$/PMN-xPT[28,29] heterostructures where the properties of oxide films are exclusively modified by the electric-field-induced strain in PMN-xPT via ferroelectric domain switching. However, it still remains elusive whether or not the electric-field-induced interfacial electric charges could strongly modify the charge carrier density and subsequently the physical properties of oxide films with relatively low carrier density (10^{18}–10^{19} cm^{-3}). Moreover, for the oxide film/FE crystal heterostructures, which order parameter (strain or electric charge) is more important in controlling the properties of oxide films has yet to be well understood since the strain effect and the charge effect coexist and both effects could affect the films' properties. A clear understanding of the roles played by the poling-induced strain effect and charge effect and the ways discriminating these effects would therefore help to understand the essential physics of oxide film/FE crystal heterostructures and the design of FE crystal-based magnetoelectric electronic devices.

On the basis of the above considerations, we have fabricated ferroelectric FETs by epitaxially growing hexagonal ZnO:Mn (a = 3.25 Å, c = 5.2 Å) thin films on (111)-oriented 0.71PMN-0.29PT (PMN-PT) ($a{\approx}b{\approx}c{\approx}4.02$ Å) single-crystal substrates and studied the interfacial charge effect in these semiconductor film/PMN-PT heterostructures with the charge carrier density of the semiconductor film being 2–3 order lower than that of $La_{0.7}Sr_{0.3}CoO_3$ and $La_{1-x}A_xMnO_3$ (A = Ca, Sr, Ba) films. We have realized charge-mediated nonvolatile electric-field-control of electronic transport and magnetic properties at room temperature for the first time for PMN-PT single-crystal-based heterostructures and achieved a significant carrier concentration-tunability of resistance [i.e., $(\Delta R/R)/(\Delta n/n)$] and magnetization [i.e., $(\Delta M/M)/(\Delta n/n)$] by ≈400% and ≈257%, respectively, at room temperature, which could be used to encode information to obtain four logic states or achieve storing information magnetically and reading it out electrically. More importantly, we disclosed the relative importance of the strain effect and the interfacial charge effect in oxide film/PMN-PT crystal heterostructures and the ways to tune them, which should be valuable in view of the engineering of PMN-PT single-crystal-based heterostructures for application in oxide electronic devices.

2. Results and Discussion

The out-of-plane orientation and phase purity of the ZnO:Mn film were characterized by x-ray diffraction (XRD) θ–2θ scans. **Figure 1**a shows that the c-axis of the film is perpendicular to the growth plane of the PMN-PT(111) substrate and no diffraction peaks indicative of other orientations or impurities were found, suggesting that the ZnO:Mn film is single phase with hexagonal wurtzite structure. XRD rocking curve taken on the ZnO:Mn(0002) diffraction peak has a full width at half maximum of 0.8° (Figure S2, Supporting Information). AFM measurements revealed that the ZnO:Mn films have a flat surface with a root-mean-square roughness of ≈1.2 nm (inset of Figure 1a). In order to establish the in-plane epitaxial relationship between the ZnO:Mn film and the PMN-PT(111) substrate, we performed ϕ scans which were taken on the ZnO:Mn (10–11) and PMN-PT(001) diffraction peaks and present the results in Figure 1b. As can be seen, only six peaks 60° apart from each other were observed for the ZnO:Mn (10–11) family with six crystal planes intersecting the surface at the same angle of 61.61°, revealing good epitaxy of the ZnO:Mn film on the PMN-PT substrate. From the relative position of the ZnO:Mn (10–11) (2θ = 36.5°, χ = 61.61°) and PMN-PT (001) (2θ = 45°, χ = 35.26°), the in-plane orientation relationship obtained is ⟨11–20⟩ ZnO:Mn‖⟨0–11⟩ PMN-PT, with the in-plane atomic arrangement shown in Figure 1d. The lattice mismatch $\left(\frac{\sqrt{3}a_{\text{ZnO:Mn}}-\sqrt{2}a_{\text{PMN-PT}}}{\sqrt{2}a_{\text{PMN-PT}}}\right)$ along the direction of ⟨11–20⟩ ZnO:Mn is –0.98%.

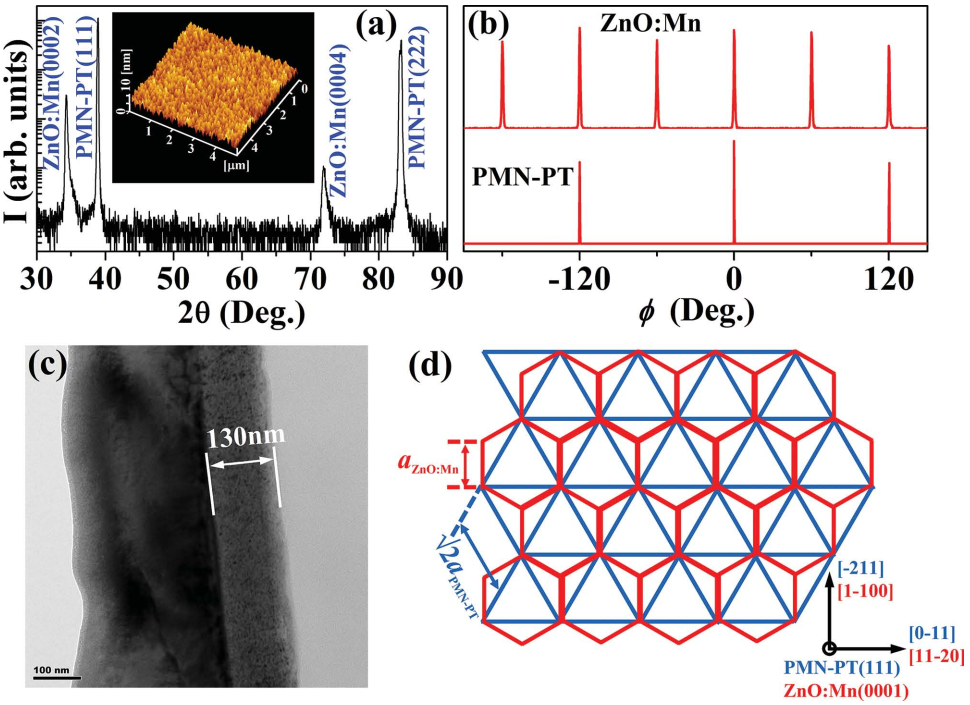

Figure 1. a) XRD θ–2θ scan pattern for the ZnO:Mn/PMN-PT heterostructure; (inset) the AFM image of the ZnO:Mn film. b) XRD phi scan patterns taken on the ZnO:Mn(10–11) and PMN-PT(001) diffraction peaks, respectively. c) Low-magnification cross-sectional TEM image of the ZnO:Mn/PMN-PT structure. d) Illustration of in-plane lattice arrangements for hexagonal ZnO:Mn unit cells on PMN-PT(111) substrate.

Cross-sectional transmission electron microscopy (TEM) studies were conducted on the interface of the ZnO:Mn/PMN-PT heterostructure. The low-magnification image in Figure 1c reveals the uniform thickness (≈130 nm) of the film and a clearly defined interface. A representative high-resolution transmission electron microscopy (HRTEM) image of the as-grown sample is shown in **Figure 2**a, where the distance between neighboring crystal planes in the left- and right-hand sides are ≈0.23 and ≈0.26 nm, corresponding to the PMN-PT(111) and ZnO:Mn(0002) planes, respectively. No Mn metal or Mn-rich wurtzite clusters could be found according to the HRTEM images taken at a number of locations throughout the cross sectional region, implying that the Mn dopants have dissolved homogenously into the ZnO matrix. The elemental mapping of the film surface also reveals a uniform distribution of Mn (see Figure S4, Supporting Information), further confirming the single-phase characteristic of the ZnO:Mn film. HRTEM images also reveal an ordered structure of the ZnO:Mn film with the *c*-axis perpendicular to the substrate plane. Figure 2b shows a selected area electron diffraction (SAED) pattern, taken from both the ZnO:Mn film and PMN-PT substrate along the [1–100] direction of the ZnO:Mn film (or [–211] direction of the PMN-PT substrate. The obtained orientation relationship between the ZnO:Mn film and the PMN-PT substrate is fully consistent with the XRD analysis. The above microscopic characterizations show that the ZnO:Mn film has a high degree of crystallinity and atomically smooth interface, which are both important parameters since the field effect mostly occurs near the interface. X-ray photoelectron spectroscopy (XPS) measurements (see Figure S2, Supporting Information) show that the Mn 2*p*3/2 and Zn 2*p*3/2 peaks were located at 640.9 and 1022.1 eV, respectively, indicating that Mn and Zn ions are mainly in the chemical states of Mn^{2+} and Zn^{2+}.[30] The average manganese content determined by the EDS measurements (see Figure S3, Supporting Information) is ≈4.28%, close to the nominal Mn doping level (5%) of the PLD target.

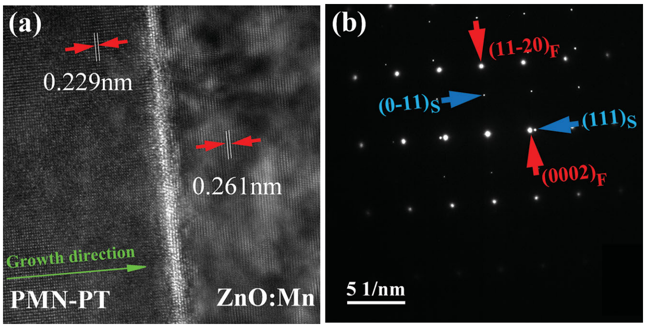

Figure 2. a) HRTEM image and b) SAED pattern taken at the interface for the ZnO:Mn/PINT(111) heterostructure.

The chemical composition of the PMN-PT substrates used in the present work locates within the rhombohedral phase region of the phase diagram, of which the spontaneous polarization is along eight body diagonals of the pseudocubic unit cell with *R*3*C* symmetry at room temperature. Piezoresponse force microscopy (PFM) was used to image the evolution of ferroelectric domains under different polarization states with the cantilever along the [–101] direction. For a scan direction along [–101], it is sensitive to the in-plane polarization projection along the [–12–1] direction.[7] As is evident from the schematics shown in the top row of Figure S5 (Supporting Information) this

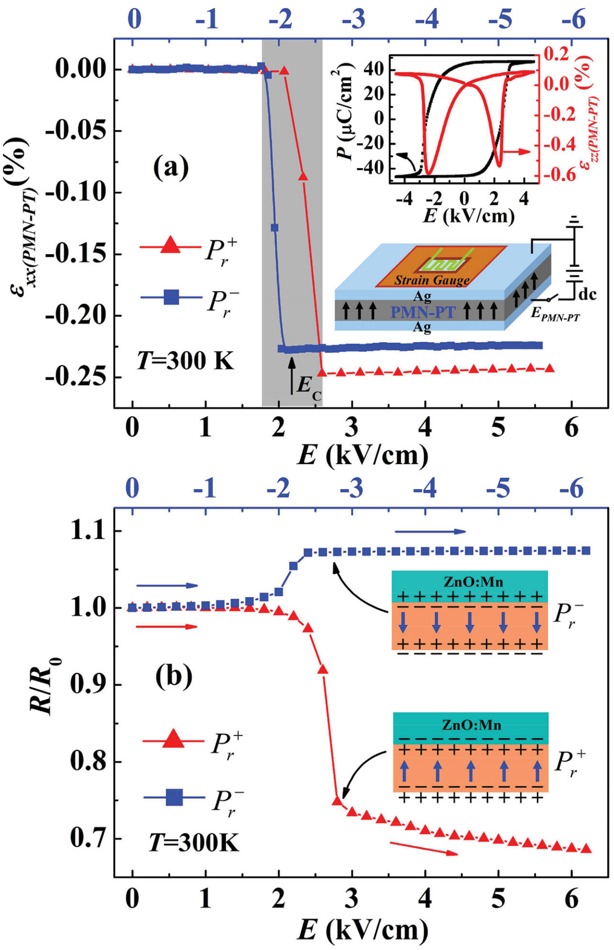

Figure 3. a) Electric-field-induced in-plane strain of the PMN-PT substrate during the positive and negative poling processes. (Insets) Polarization and strain versus E-field (bipolar) curves for a PMN-PT substrate (upper panel) and the schematic of the experimental setup for measuring electric-field-induced in-plane strain of the PMN-PT substrate (lower panel). b) The evolution of the film resistance with electric field during the positive and negative poling processes of the PMN-PT substrates. Insets illustrate the accumulation/depletion of electron carriers due to the ferroelectric field effect.

component of polarization is zero only when the polarization lies perpendicular to the sample surface. For the unpoled PMN-PT, the polarization vectors point along the eight body diagonals randomly (Figure S5a, Supporting Information), resulting in the PFM phase images with a mixture of out-of-plane and in-plane domains (Figure S5b, c, Supporting Information). When a poling voltage of –6 V was applied to the tip, all polar vectors rotated downward in the poled area (blue box), pointing along the [–1–1–1] direction (Figures S5d,e Supporting Information) with no in-plane component along the [–12–1] direction and thus, no contrast could be seen within the blue box of the in-plane image in Figure S5f (Supporting Information). When a subsequent dc voltage of +6 V was applied, all out-of-plane polarizations previously pointing toward the [–1–1–1] direction are now reversed (Figure S5h, Supporting Information) with the in-plane polarization remaining zero (Figure S5i, Supporting Information). In other words, a 180° domain switching has occurred.

The inset (upper panel) of **Figure 3**a presents a typical rectangular shaped polarization–electric field (*P*–*E*) hysteresis loops with a remnant polarization $P_r \approx 45$ µC cm^{-2} and a well-defined butterfly shaped strain versus electric field (ε–*E*) loop of a PMN-PT substrate measured by the TF Analyzer 2000 (aixACCT) measurement system. Note that the *P*–*E* loop is asymmetric while the ε–*E* loop is symmetric with respect to the sign of the applied electric field. The fundamentally different shapes between the *P*–*E* loop and the ε–*E* loop can be used to distinguish which effect (i.e., the ferroelectric field effect or the strain effect) exerts influence on the modulation of physical properties of ZnO:Mn films. The above discussed domain configuration and the switching category reasonably account for the large remnant polarization ($P_r \approx 45$ µ cm^{-2}) and equivalent strain states (i.e., $\varepsilon_{zz(\text{PMN-PT})} = 0$) after 180° polarization switching, and will be discussed further in the following sections. These features highlight the extraordinary nature of the rhombohedral PMN-PT(111) in comparison with others.

In order to observe the effects of substrate poling along the ⟨111⟩ crystal direction on the electronic transport properties of the ZnO:Mn film, the resistance of the film was measured at room temperature as a function of applied gate electric field (*E*) for two ZnO:Mn/PMN-PT samples with a size of 5 × 5 × 0.5 mm^3 using the experimental setup shown in Figure S1a (Supporting Information). Note that the two ZnO:Mn/PMN-PT samples were cut from the same piece of sample with a size of 10 × 5 × 0.5 mm^3. Initially, the PMN-PT substrate was in the unpoled P_r^0 state and *E* was increased from 0 to 6.2 kV cm^{-1} (or –6.2 kV cm^{-1}) at an interval of 0.2 kV cm^{-1} (or –0.2 kV cm^{-1}). The ZnO:Mn is a *n*-type material, so the majority of charge carriers in the channel are electrons. The application of a positive electric bias through the top and bottom electrodes polarizes the PMN-PT substrate such that the polarization direction points toward the ZnO:Mn film (denoted by P_r^+). This polarization rearrangement effectively induces negative charges at the interface, thereby accumulating the channel with electron carriers. By contrast, for the other unpoled ZnO:Mn/PMN-PT sample, the application of a negative electric bias poled the PMN-PT negatively (i.e., polarization direction points toward bottom Au electrode, denoted by P_r^-) and thus depletes electron carriers in the ZnO:Mn channel. As can be seen in Figure 3b, the resistance of the ZnO:Mn/PMN-PT FET indeed behaves as expect when the modulation is a result of the ferroelectric field effect: the channel resistance decreases upon positive poling and increases upon negative poling, as in stark contrast to $La_{1-x}(Ca,Sr,Ba)_xMnO_3$/PMN-*x*PT,[8,9,11,15,22,23] $La_{0.7}Sr_{0.3}CoO_3$/PMN-*x*PT,[21] VO_2/PMN-*x*PT,[24,25] Fe_3O_4/PMN-*x*PT,[7] $CoFe_2O_4$/PMN-*x*PT,[26,27] and $BiFeO_3/La_{0.7}Sr_{0.3}MnO_3$/PMN-*x*PT[28,29] systems where the domain-switching-induced strain plays a dominant role at room temperature. It should be pointed out that whether the PMN-PT was poled positively or negatively, the 71°/109° ferroelectric domain switching exclusively induces in-plane compressive strain, as shown in Figure 3a. There is no doubt that the polarity independent strain versus *E* curves (red and blue) fails to explain the polarity dependent resistance variation, further ruling out the possible strain-mediated

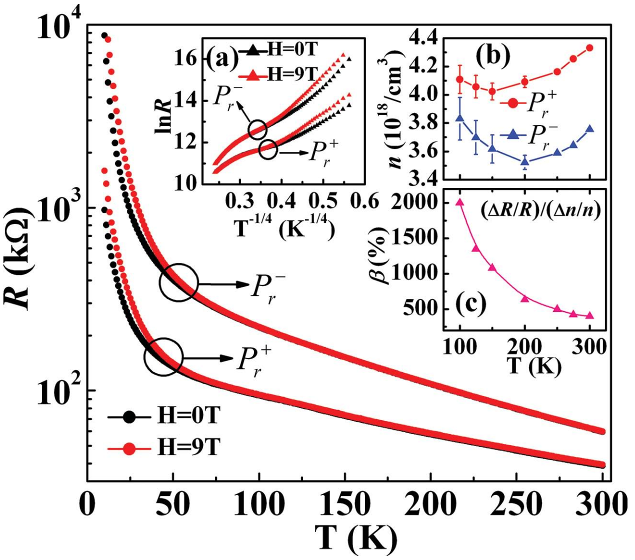

Figure 4. Temperature dependence of the resistance for the ZnO:Mn film for the P_r^+ and P_r^- states, as measured with the magnetic field $H = 0$ and 9 T applied perpendicularly to the film plane. a) ln$R$ versus $T^{-1/4}$ curves. b) Carrier density n of the ZnO:Mn film at various temperatures when the PMN-PT substrate was in the P_r^+ and P_r^- states, respectively. c) Temperature dependence of the carrier concentration-tunability of resistance for the ZnO:Mn film.

coupling mechanism in the ZnO:Mn/PMN-PT system. Note that the slight discrepancy in the coercive field for the positive and negative poling could be due to the intrinsic compositional inhomogeneity (i.e., the segregation of $PbTiO_3$) along the growth direction for relaxor ferroelectric single crystals grown by a modified Bridgman technique.[31]

Figure 4 shows the resistance versus temperature for the ZnO:Mn channel measured in a zero magnetic field and a magnetic field of $H = 9$ T for both directions of the ferroelectric polarization in the PMN-PT substrate. The results disclose a clear correlation of the resistance with the polarization state in the PMN-PT. Over the entire temperature region, the resistance for the P_r^+ state is smaller than that for the P_r^- state. Associated with the polarization switching from P_r^+ to P_r^-, the relative change in the resistance, defined as $\Delta R/R = [R(P_r^-) - R(P_r^+)]/R(P_r^+)$, reaches 53% at 300 K and increases to 795% at 10 K. We note that this resistance modulation is reversible and nonvolatile upon cycling the two polarization state. Hereafter, we refer to the high- and low-resistance states as "ON" and "OFF" states, respectively. We further determined the electron concentration n through measuring the Hall effects of the device using the Van de Pauw configuration shown in Figure S1a (Supporting Information). The Hall coefficient R_H is negative for all temperatures, revealing the electron-doping nature of the ZnO:Mn film. The calculated average n for both P_r^+ and P_r^- states are plotted against temperature in the inset b) of Figure 4. Clearly, the accumulation or depletion of electron carriers by the ferroelectric field effect can plausibly account for the significant modification of the resistance. Using the resistance and carrier concentration data, the carrier concentration-tunability of resistance β, defined as $\beta = |(\Delta R/R)/(\Delta n/n)|$ where $\Delta n/n = [n(P_r^-) - n(P_r^+)]/n(P_r^+)$, was calculated and presented in the inset c) of Figure 4. β reaches 400% at 300 K and increases to 2000% at 100 K, suggesting that the electronic transport properties are highly sensitive to the carrier concentration. Note that these values are much larger than that of FETs based on perovskite transition-metal oxide films (e.g., $La_{0.8}Ca_{0.2}MnO_3$, $SrRuO_3$) and $Pb(Zr_{1-x}Ti_xO_3)$.[32,33] Such charge-mediated nonvolatile modulation of resistance is also much more effective than that of strain-mediated nonvolatile modulation[7,11,24] for PMN-PT single-crystal-based oxide heterostructures, demonstrating the advantage of the device.

In order to achieve greater resistance modulation, the number of electron carriers per unit area in the semiconductor film should not be too large with respect to the amount of available two-dimensional electric charge produced by the ferroelectric gate. A typical carrier density of 4×10^{18} cm^{-3} (inset b) of Figure 4) equals to an areal density of 5.2×10^{13} cm^{-2} for the 130 nm thick film. Thus, a large screening length and prominent field effects are therefore expected. However, the actual largest average change in the areal density ($\Delta n_{3D} \times t_{ZnO:Mn}$) over a thickness of 130 nm is calculated as only 0.79×10^{13} cm^{-2} at 275 K, which could probably be attributed to the relatively large film thickness ($t_{ZnO:Mn} = 130$ nm).[34] For a thinner ZnO:Mn film grown on PMN-PT(111), we indeed observed a larger $\Delta R/R$ upon polarization reversal, which will be discussed in the following section. It should be noted that no clear association between the ferroelectric field effect and the electron mobility has been found for the present ZnO:Mn/PMN-PT system.

A more direct visualization of the ferroelectric field effect can be seen in **Figure 5**a, where the resistance of the ZnO:Mn film was measured against bipolar electric field applied to the PMN-PT gate at $T = 300$ K. The resistance was switched hysteretically between two distinctive values in response to the polarization reversal. This characteristic, commensurate with the P-E loop of the PMN-PT substrate (inset of Figure 3a), shows that the distinct difference in the resistance at $E = 0$ kV cm^{-1} tracks the switching of the polarization direction in terms of nonvanishing influence of the induced interfacial electric charge from ferroelectric polarization. By decreasing the film thickness to ≈42 nm, we achieved a larger polarization-reversal-induced resistance modulation (see Figure S6, Supporting Information), implying greater interfacial electric charge effect for thinner ZnO:Mn films. Further, attribution of resistance change to strain can be precluded from symmetry consideration as strain effect should yield $R(E)$ loop with even symmetry pertaining to $E = 0$ kV cm^{-1}.[9,15,23] This point is further corroborated by in situ XRD θ–2θ scans which denote no shift in the PMN-PT(111) and ZnO:Mn(0002) diffraction peaks (Figure 5c) upon polarization reversal. The well-saturated resistance hysteresis loop implies that the channel resistance can be switched between two stable states by applying pulse electric field E ($E > E_C$) to the gate layer. Upon the application of a positive dc electric field (e.g., 6 kV cm^{-1}), the "ON" state with P_r^- and R_{ON} can be switched back to "OFF" state with P_r^+ and R_{OFF}, which persists until a negative pulse field was applied. The process of controllable switching of the resistance by a sequence of negative/positive pulse cycles is presented in Figure 5b, revealing reversible, nonvolatile and reproducible electric-field controlled modulation of the process.

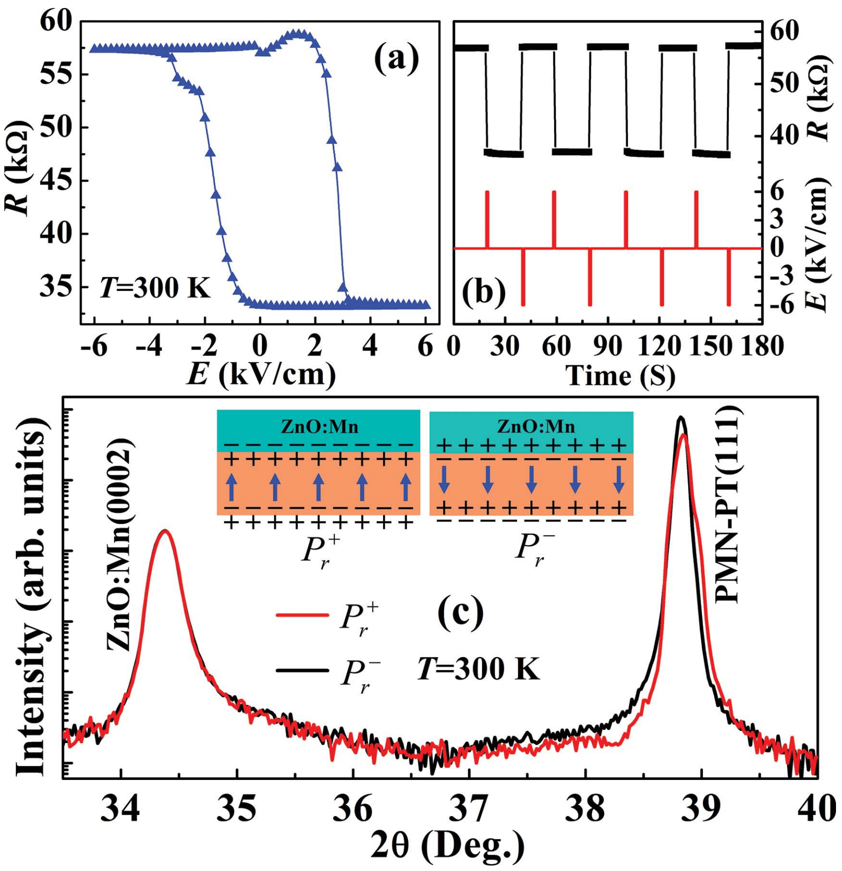

Figure 5. a) Variation of the film resistance with bipolar electric field applied across the ZnO:Mn/PMN-PT heterostructure at room temperature. b) Nonvolatile resistance switching of the ZnO:Mn film by a sequence of pulse electric field at room temperature. c) XRD θ–2θ scan patterns in the vicinity of ZnO:Mn(0002) and PMN-PT(111) diffraction peaks under two distinct polarized states of the PMN-PT substrate. Insets show schematic of the polarization direction for the P_r^+ and P_r^- states.

Magnetotransport measurement is an effective approach to understand doping-modified magnetic interactions in transition-metal doped ZnO. **Figure 6** shows the dependence of magnetoresistance (MR) on electron concentration n at several fixed temperatures as stated. MR is defined as $\mathrm{MR} = [R(H) - R(0)] / R(0)$, where $R(H)$ and $R(0)$ are the resistance in the presence and absence of a magnetic field H, respectively. For the P_r^- state, at a low temperature, such as $T = 10$ K, MR is positive and increases sharply with increasing magnetic field from $H = 0$ to 3 T before showing a trend to saturate in higher field ($H > 3$ T) with MR value close to 80% for the maximum field of $H = 9$ T. The positive MR decreases drastically with increasing temperature and changes its sign near 100 K where only a small negative MR (–0.5%) was observed. Normally, the doping of 3*d* transition metal would induce strong *s*–*d* exchange interaction in magnetic oxide semiconductors. In the presence of a magnetic field, the *s*-type conduction band will split into two subbands corresponding to two spin orientations, thus causing a transfer of electrons from the high-energy subband to the other.[35] The positive MR probably originates from the magnetic scattering of spin polarized conducting electrons due to the magnetic field-induced redistribution of electrons.[36] The temperature dependent crossover from positive MR to negative MR can be explained as a result of decreasing splitting between the spin polarized subbands with increasing temperature, causing the negative *MR* becomes more pronounced at high temperatures.[37] Currently, the underlying physical origin of the negative MR is still under debate and yet to be determined. The present small negative MR might be resulted from the formation of magnetic polarons (MP).[38] The exchange coupling of doped magnetic ions in MPs could be indirectly induced by localized carriers. The spins of the doped magnetic ions tend to be aligned parallel in a magnetic field, resulting in reduced magnetic scattering of conducting electrons.

Comparing MR values for different polarized states, an appreciable drop was found when the polarization state was switched from P_r^- to P_r^+, namely, the positive MR decreases with increasing electron concentration n in relation to the decreasing spin polarization;[35] while the negative MR at $T = 100$ K remains almost unchanged upon polarization reversal. This strong electron concentration dependent magnetotransport property supports the results reported by Xu *et al.*,[36,39] who systematically adjusted the electron concentration by varying oxygen pressure, substrate temperature, and film thickness during film deposition. Advantageously, our FET structure enables in situ continuous and reversible tuning of carrier density, which is encouraging from fundamental perspectives, as it provides a clean way to tune carrier concentration and thus avoids the effects of doping-induced lattice distortion and disorder as well as the variation of oxygen content from sample to sample.

The polarization-reversal-induced interfacial electric charge not only influences the electronic transport but also has a significant impact on the ferromagnetism of the ZnO:Mn film. In **Figure 7**, we present the room-temperature magnetization–magnetic field (M–H) hysteresis loops for two consecutive cycles of P_r^+ and P_r^- states of the PMN-PT substrate. Note that the diamagnetic contribution from the substrate has been subtracted from the raw magnetic data shown in the inset a) of Figure 7. Remarkably, the ZnO:Mn/PMN-PT exhibits room temperature ferromagnetic behavior for both the P_r^+ and P_r^- states, which is clearly illustrated by the coercive field, remanence, and relatively low saturation field. After measurements of the M–H hysteresis loops for the P_r^+ and P_r^- states, we removed the ZnO:Mn film from the substrate and then measured the M–H hysteresis loop of the same piece of bare PMN-PT. As can be seen in the inset b) of Figure 7, the PMN-PT is essentially diamagnetic, thus firmly establishing that the ferromagnetism of the ZnO:Mn/PMN-PT heterostructure comes from the ZnO:Mn film. The most eminent feature observed here is

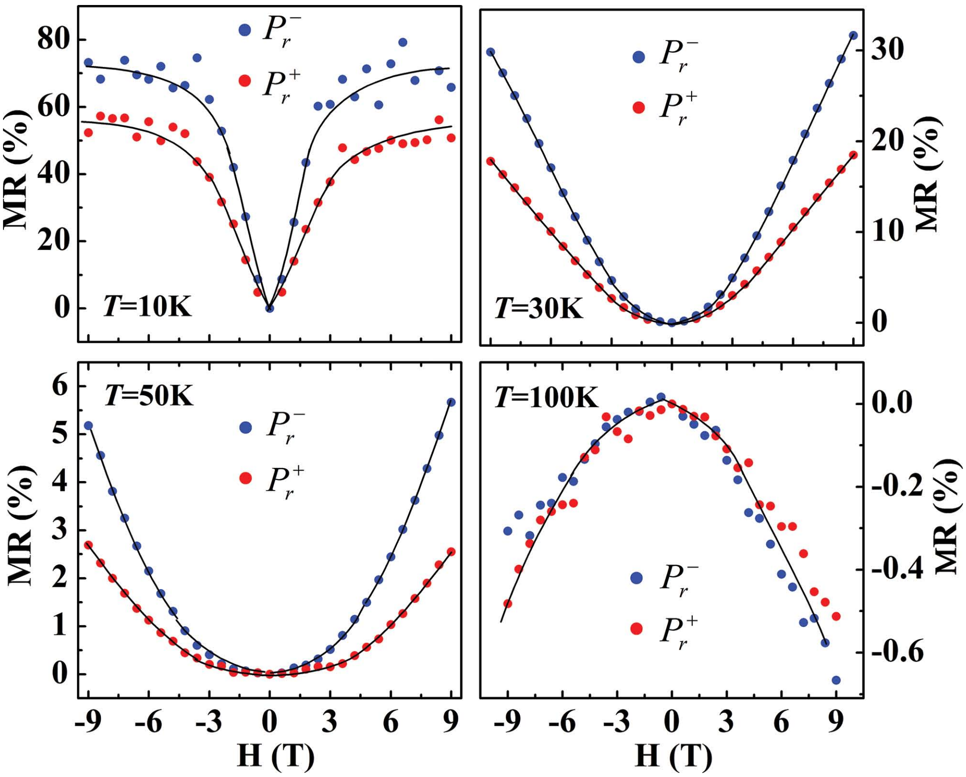

Figure 6. Magnetoresistance of the ZnO:Mn film for the P_r^+ and P_r^- state, measured at the temperatures as stated.

that the polarization-reversal-induced accumulation/depletion of electron carriers has a profound influence on the saturation magnetization (M_S) of the ZnO:Mn film. At room temperature, M_S decreases by ≈34% with increasing carrier concentration from 3.76×10^{18} cm^{-3} for the P_r^- state to 4.33×10^{18} cm^{-3} for the P_r^{+} state. The figure of merit that characterizes the effectiveness of the carrier concentration-tunability of magnetization is $(\Delta M/M)/(\Delta n/n) \approx 257\%$. Actually, the ZnO:Mn/PMN-PT heterostructure can also be viewed as an artificially structured multiferroic composite that combines dissimilar magnetic (ZnO:Mn) semiconductor with ferroelectric (PMN-PT) single crystal systems. This gate-tunable ferromagnetism is equivalent to the charge-mediated converse magnetoelectric coupling,[40] thus linking the emerging field of multiferroics with conventional semiconductor microelectronics.

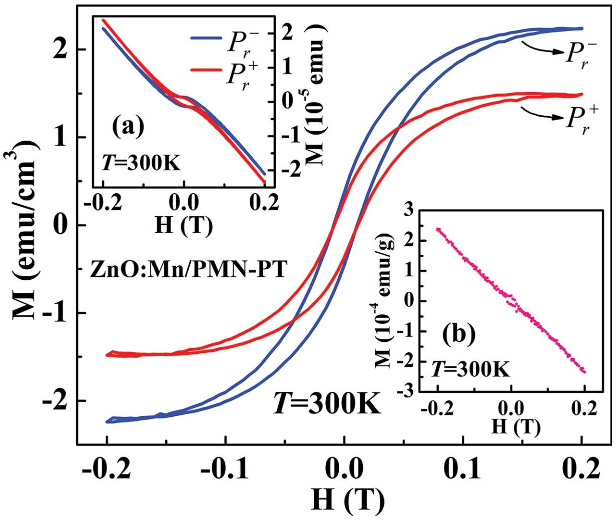

Figure 7. Magnetization versus magnetic field (M–H) hysteresis loops of the ZnO:Mn film after the subtraction of the diamagnetic contribution from the PMN-PT substrate. Inset a): M–H hysteresis loops of the ZnO:Mn/PMN-PT sample before the subtraction of the diamagnetic contribution from the PMN-PT substrate. Inset b): M–H hysteresis loops of the PMN-PT single crystal after the removal of the ZnO:Mn film.

Based on the resistance data shown in the inset a) of Figure 4, it is found that the electronic transport of the ZnO:Mn film obeys the Mott formula, $R = A\exp(T_0/T)^{1/4}$, in the low temperature limit with the fitting parameter T_0 well above 10 000 K, meeting requirement for the occurrence of ferromagnetism at room temperature.[41] From the slope of the linear fitting curves, T_0 for the P_r^- state is pretty larger than that for the P_r^+ state; our results are in full accordance with ref. [40], where it was reported that the magnetization increases with T_0. The magnetic polaron theory proposed by Coey *et al.*[42] gives one plausible explanation for the inverse correlation between the magnetization and the electron density as controlled by the ferroelectric field effect. Specifically, an electron associated with a particular defect is confined in a hydrogenic orbital. Overlap between a hydrogenic electron and the *d*-shell orbitals of the magnetic dopant leads to a cooperative percolative ordering of such magnetic ions. Each local magnetic moment is the effective magnetic polaron and ferromagnetism occurs when the polaronic density reaches the percolation limit. If the shape of the corresponding wave function of the magnetic polaron changes suddenly due to the hopping of a mobile carrier, the time-dependent exchange field may disturb the spin of the magnetic ion and hence suppress the magnetism. In this regard, the decrease in the magnetization upon increase in carrier density of the ZnO:Mn film could be reasonably understood.

3. Conclusions

In summary, we reported the first successful epitaxial growth of hexagonal ZnO:Mn semiconductor thin films on high performance perovskite PMN-PT single crystals and realized unprecedented charge-mediated electric-field control of both electronic transport and ferromagnetism at room temperature for PMN-PT single-crystal-based oxide heterostructures. We further disclosed the relative importance of the strain effect and interfacial charge effect in oxide film/FE crystal heterostructures and the ways to tune them by appropriately adjusting the charge carrier density of the films. Taking into account the carrier accumulation/depletion by the ferroelectric polarization, an electrostatic model well explains the electric polarization driven modulation of the electronic transport, magnetotransport, and ferromagnetism. Our results establish important advances toward the implementation of intrinsic doping-dependence of physical properties in DMS. The successful integration of dilute magnetic semiconductor with high piezoelectrically active PMN-PT single crystal offers a promising technology for application in future hybrid electronic devices operating at room temperature with lower dissipation and high sensitivity by utilizing both piezostrain and gate-tunable magnetization and resistance.

4. Experimental Section

Film Growth: High quality ZnO:Mn films were grown on one-side-polished and (111)-oriented $0.71\text{Pb}(\text{Mg}_{1/3}\text{Nb}_{2/3})\text{O}_3$–$0.29\text{PbTiO}_3$ single-crystal substrates by pulsed laser deposition (PLD) from a high purity ZnO:Mn ceramic target. The target was ablated using a KrF excimer laser (248 nm) with a pulse energy density of 2 J cm^{-2} and a repetition rate of 3 Hz. The growth was carried out in 0.01 Pa oxygen pressure at 600 °C. The as-grown films were annealed in situ for 30 min then cooled to room temperature at a rate of 5 °C min^{-1}. The film thickness was controlled by the number of laser pulses.

Structure Characterization: The crystal structure of the ZnO:Mn film and the epitaxial relationship between the ZnO:Mn film and the PMN-PT substrate were characterized by a high resolution four-circle Bruker D8 Discover X-ray diffractometer equipped with Cu $K_{\alpha1}$ radiation ($K_{\alpha1} = 1.5406$ Å) and a high-resolution transmission electron microscope (TEM) (Tecnai G2 F20 S-Twin), respectively. The chemical states of manganese ions were studied by ESCAlab250 X-ray photoelectron spectroscope. The elemental distribution and film composition was determined by the energy dispersive spectroscopic (EDS) mapping (Magellan 400 scanning electron microscope). The surface morphology and thickness of the films were observed by an atomic force microscope (Nanocute SII, Seiko, Japan) and a Magellan 400 scanning electron microscope, respectively. PFM measurements were made with a Veeco NanoScope-IV Multimode AFM under ambient conditions.

Electronic Transport and Magnetic Properties Measurements: The in-plane transport properties of the ZnO:Mn films were studied via the Van de Pauw configuration using a PPMS (physical property measurement system, PPMS-9, Quantum Design) with the magnetic field applied perpendicular to the film plane, at temperatures ranging from 10 to 300 K. Magnetic properties of the films were measured using a SQUID (superconducting quantum interference device, MPMS3, Quantum Design) magnetometer with the magnetic field applied parallel to the film plane.

Supporting Information

Supporting Information is available from the Wiley Online Library or from the author.

Acknowledgements

This work is supported by the National Natural Science Foundation of China (Grant Nos. 51172259, 51428202, 51332007, and 11090332), National Basic Research Program of China (Grant Nos. 2012CB922003 and 2015CB921201), and the CAS/SAFEA International Partnership Program for Creative Research Teams. The work at Beijing Normal University is supported by NSFC (Grant Nos. 51332001, 51322207, and 11274045).

Received: October 27, 2014
Revised: December 1, 2014

[1] D. Pantel, S. Goetze, D. Hesse, M. Alexe, *Nat. Mater.* **2012**, *11*, 289.
[2] M. Liu, Z. Y. Zhou, T. X. Nan, B. M. Howe, G. J. Brown, N. X. Sun, *Adv. Mater.* **2013**, *25*, 1435.
[3] M. Liu, B. M. Howe, L. Grazulis, K. Mahalingam, T. X. Nan, N. X. Sun, G. J. Brown, *Adv. Mater.* **2013**, *25*, 4886.
[4] S. Zhang, Y. G. Zhao, P. S. Li, J. J. Yang, S. Rizwan, J. X. Zhang, J. Seidel, T. L. Qu, Y. J. Yang, Z. L. Luo, Q. He, T. Zou, Q. P. Chen, J. W. Wang, L. F. Yang, Y. Sun, Y. Z. Wu, X. Xiao, X. F. Jin, J. Huang, C. Gao, X. F. Han, R. Ramesh, *Phys. Rev. Lett.* **2012**, *108*, 137203.
[5] J. T. Heron, M. Trassin, K. Ashraf, M. Gajek, Q. He, S. Y. Yang, D. E. Nikonov, Y. H. Chu, S. Salahuddin, R. Ramesh, *Phys. Rev. Lett.* **2011**, *107*, 217202.
[6] R. O. Cherifi, V. Ivanovskaya, L. C. Phillips, A. Zobelli, I. C. Infante, E. Jacquet, V. Garcia, S. Fusil, P. R. Briddon, N. Guiblin, A. Mougin, A. A. Unal, F. Kronast, S. Valencia, B. Dkhil, A. Barthelemy, M. Bibes, *Nat. Mater.* **2014**, *13*, 345.
[7] T. X. Nan, Z. Y. Zhou, J. Lou, M. Liu, X. Yang, Y. Gao, S. Rand, N. X. Sun, *Appl. Phys. Lett.* **2012**, *100*, 132409.
[8] M. Liu, J. Hoffman, J. Wang, J. X. Zhang, B. Nelson-Cheeseman, A. Bhattacharya, *Sci. Rep.* **2013**, *3*, 1876.
[9] M. C. Dekker, A. Herklotz, L. Schultz, M. Reibold, K. Vogel, M. D. Biegalski, H. M. Christen, K. Dörr, *Phys. Rev. B* **2011**, *84*, 054463.
[10] Q. X. Zhu, M. Zheng, M. M. Yang, X. M. Li, Y. Wang, X. Shi, H. L. W. Chan, H. S. Luo, X. G. Li, R. K. Zheng, *Appl. Phys. Lett.* **2013**, *103*, 132910.
[11] Y. J. Yang, Z. L. Luo, M. M. Yang, H. L. Huang, H. B. Wang, J. Bao, G. Q. Pan, C. Gao, Q. Hao, S. T. Wang, M. Jokubaitis, W. Z. Zhang, G. Xiao, Y. P. Yao, Y. K. Liu, X. G. Li, *Appl. Phys. Lett.* **2013**, *102*, 033501.
[12] J. Hoffman, X. A. Pan, J. W. Reiner, F. J. Walker, J. P. Han, C. H. Ahn, T. P. Ma, *Adv. Mater.* **2010**, *22*, 2957.
[13] C. H. Ahn, J. M. Triscone, J. Mannhart, *Nature* **2003**, *424*, 1015.
[14] C. H. Ahn, S. Gariglio, P. Paruch, T. Tybell, L. Antognazza, J. M. Triscone, *Science* **1999**, *284*, 1152.
[15] R. K. Zheng, Y. Wang, J. Wang, K. S. Wong, H. L. W. Chan, C. L. Choy, H. S. Luo, *Phys. Rev. B* **2006**, *74*, 094427.
[16] H. J. A. Molegraaf, J. Hoffman, C. A. F. Vaz, S. Gariglio, D. van der Marel, C. H. Ahn, J.-M. Triscone, *Adv. Mater.* **2009**, *21*, 3470.

[17] D. Yi, J. Liu, S. Okamoto, S. Jagannatha, Y.-C. Chen, P. Yu, Y.-H. Chu, E. Arenholz, R. Ramesh, *Phys. Rev. Lett.* **2013**, *111*, 127601.
[18] Y. W. Yin, J. D. Burton, Y.-M. Kim, A. Y. Borisevich, S. J. Pennycook, S. M. Yang, T. W. Noh, A. Gruverman, X. G. Li, E. Y. Tsymbal, Q. Li, *Nat. Mater.* **2013**, *12*, 397.
[19] P. Sharma, A. Gupta, K. V. Rao, F. J. Owens, R. Sharma, R. Ahuja, J. M. O. Guillen, B. Johansson, G. A. Gehring, *Nat. Mater.* **2003**, *2*, 673.
[20] S. Mathews, R. Ramesh, T. Venkatesan, J. Benedetto, *Science* **1997**, *276*, 238.
[21] A. D. Rata, A. Herklotz, K. Nenkov, L. Schultz, K. Dörr, *Phys. Rev. Lett.* **2008**, *100*, 076401.
[22] J. F. Wang, Y. C. Jiang, Z. P. Wu, J. Gao, *Appl. Phys. Lett.* **2013**, *102*, 071913.
[23] T. Jiang, S. W. Yang, Y. K. Liu, Y. W. Yin, S. N. Dong, W. B. Zhao, X. G. Li, *Appl. Phys. Lett.* **2013**, *103*, 053504.
[24] B. W. Zhi, G. Y. Gao, H. R. Xu, F. Chen, X. L. Tan, P. F. Chen, L. F. Wang, W. B. Wu, *ACS Appl. Mater. Interfaces* **2014**, *6*, 4603.
[25] T. X. Nan, M. Liu, W. Ren, Z. G. Ye, N. X. Sun, *Sci. Rep.* **2014**, *4*, 5931.
[26] H. Ding, J. W. Cheah, L. Chen, T. Sritharan, J. L. Wang, *Thin Solid Films* **2012**, *522*, 420.
[27] Z. G. Wang, Y. Zhang, R. Viswan, Y. X. Li, H. S. Luo, J. F. Li, D. Viehland, *Phys. Rev. B* **2014**, *89*, 035118.
[28] M. M. Yang, X. Q. Zhao, J. Wang, Q. X. Zhu, J. X. Zhang, X. M. Li, H. S. Luo, X. G. Li, R. K. Zheng, *Appl. Phys. Lett.* **2014**, *104*, 052902.
[29] E. J. Guo, K. Dorr, A. Herklotz, *Appl. Phys. Lett.* **2012**, *101*, 242908.
[30] Y. C. Yang, F. Pan, Q. Liu, M. Liu, F. Zeng, *Nano Lett.* **2009**, *9*, 1636.
[31] Y. Y. Zhang, X. B. Li, D. A. Liu, Q. H. Zhang, W. Wang, B. R. D. Lin, X. Y. Zhao, H. S. Luo, *J. Cryst. Growth* **2011**, *318*, 890.
[32] T. Zhao, S. B. Ogale, S. R. Shinde, R. Ramesh, R. Droopad, J. Yu, K. Eisenbeiser, J. Misewich, *Appl. Phys. Lett.* **2004**, *84*, 750.
[33] C. H. Ahn, R. H. Hammond, T. H. Geballe, M. R. Beasley, J.-M. Triscone, M. Decroux, Ø. Fischer, L. Antognazza, K. Char, *Appl. Phys. Lett.* **1997**, *70*, 206.
[34] H. Yamada, M. Marinova, P. Altuntas, A. Crassous, L. Bégon-Lours, S. Fusil, E. Jacquet, V. Garcia, K. Bouzehouane, A. Gloter, J. E. Villegas, A. Barthélémy, M. Bibes, *Sci. Rep.* **2013**, *3*, 2834.
[35] T. Andrearczyk, J. Jaroszynski, G. Grabecki, T. Dietl, T. Fukumura, M. Kawasaki, *Phys. Rev. B* **2005**, *72*, 121309.
[36] Q. Y. Xu, L. Hartmann, H. Schmidt, H. Hochmuth, M. Lorenz, R. Schmidt-Grund, C. Sturm, D. Spemann, M. Grundmann, Y. Z. Liu, *J. Appl. Phys.* **2007**, *101*, 063918.
[37] Y. F. Tian, Y. F. Li, T. Wu, *Appl. Phys. Lett.* **2011**, *99*, 222503.
[38] J. Wang, Z. Gu, M. H. Lu, D. Wu, C. S. Yuan, S. T. Zhang, Y. F. Chen, S. N. Zhu, Y. Y. Zhu, *Appl. Phys. Lett.* **2006**, *88*, 252110.
[39] Q. Y. Xu, L. Hartmann, H. Schmidt, H. Hochmuth, M. Lorenz, R. Schmidt-Grund, C. Sturm, D. Spemann, M. Grundmann, *Phys. Rev. B* **2006**, *73*, 205342.
[40] J. M. Rondinelli, M. Stengel, N. A. Spaldin, *Nat. Nanotechnol.* **2008**, *3*, 46.
[41] A. J. Behan, A. Mokhtari, H. J. Blythe, D. Score, X. H. Xu, J. R. Neal, A. M. Fox, G. A. Gehring, *Phys. Rev. Lett.* **2008**, *100*, 047206.
[42] J. M. D. Coey, M. Venkatesan, C. B. Fitzgerald, *Nat. Mater.* **2005**, *4*, 173.